Plasmonically enhanced two-photon absorption induced photoacoustic microscopy with laser-synthesized TiN nanoparticles

Avishek Das, Arthur Pereira, Anton Popov, Andrei Pastukhov, Sergei Klimentov, Andrei Kabashin, Anderson Gomes

Plasmonically Enhanced Two-Photon Absorption Induced Photoacoustic Microscopy with Laser-Synthesized TiN Nanoparticles

Avishek Das [1], Arthur Cesare [1], Anton A. Popov [2], Andrei Pastukhov [3], Sergei M. Klimentov [2], Andrei V. Kabashin [3,a)], Anderson S. L. Gomes [1,2,a)]

[1]*Departamento de Física, Universidade Federal de Pernambuco, Recife, 50670-901, PE, Brazil*

[2]*MEPhI, Institute of Engineering Physics for Biomedicine (PhysBio), 31 Kashirskoe sh., 115409 Moscow, Russia*

[3]*Aix Marseille University, CNRS, LP3, 163 Ave. De Luminy, Case 917, 13288 Marseille, France*

[a)] Authors to whom correspondence should be addressed: anderson.lgomes@ufpe.br and andrei.kabashin@univ-amu.fr

ABSTRACT

Combining photonic excitation and acoustic detection, photoacoustic imaging (PAI) presents one of the most promising noninvasive biomedical diagnostic modalities, but this technique still lacks efficient nano-sized contrast agents absorbing light in the region of relative tissue transparency (630-900 nm). Here, we explore the use of titanium nitride (TiN) nanoparticles (NPs) fabricated by methods of pulsed laser ablation in liquids as a contrast agent in PAI. When prepared in acetone, the NPs are spherical, have an average size of 25 nm, and exhibit a broad plasmonic absorption peak around 700 nm. We show that solutions of these NPs render possible a strong nonlinear photoacoustic response and the generation of photoacoustic images with 67 μm resolution within the biological transparency window. The observed effect is explained by a plasmonically enhanced two-photon absorption process in TiN NPs. Combined with earlier demonstrated capability of generating photothermal therapeutic effect, relative chemical purity, and excellent biocompatibility, laser-synthesized TiN NPs promise attractive applications in biomedical theranostics involving imaging modalities based on photoacoustics microscopy or tomography.

A variety of novel optical imaging modalities beyond optical microscopes have been developed in the last decades for laboratory, preclinical and clinical diagnostic use, offering a series of unique characteristics, including non-invasiveness, high spatial resolution, controllable penetration depth, in-vivo real-time capabilities [1,2]. Among modern optical imaging modalities, prominence can be given to fluorescence imaging [3], nonlinear optical microscopy [4], optical coherence tomography [5], hyperspectral imaging [6], and photoacoustic imaging [7–10]. The impact of these optical imaging modalities has been unprecedented, although a lot of research is still being carried out aiming at further developments or exploiting multimodalities, which can benefit from the molecular specificity of each technique, as well-reviewed in ref. [11].

Owing to its high efficiency, relatively deep probing depth, and the possibility of combining with phototherapy functionality, photoacoustic imaging (PAI) presents one of the most promising modalities for biomedical theranostics [7–10]. In this modality, photons, absorbed by an endogenous or exogenous medium, induce local heating, which in turn creates an expansion/contraction of the affected region with subsequent generation of acoustic waves. While the excitation is done by the light of different wavelengths, the detection is performed using the same acoustic detector. PAI can be broadly subdivided into photoacoustic microscopy (PAM) and photoacoustic tomography (PAT) [8,9]. Furthermore, nonlinear optical processes, particularly multiphoton absorption [12] can be employed to improve the resolution, leading to the so-called nonlinear photoacoustic imaging [13].

The efficiency of PAI methods can be much improved by the employment of nanomaterials, absorbing in the region of relative tissue transparency (630-900 nm), as agents to enhance the imaging contrast. Owing to excitations of free electron oscillations (plasmons) in metals, plasmonic nanomaterials can offer orders of magnitude stronger absorption compared to conventional absorbing dyes [14], which makes them the most promising candidates for PAI and photothermal therapy modalities [15,16]. Gold (Au) nanostructures present an obvious candidate for photoacoustic imaging and other biomedical modalities, as they can combine chemical stability with strong plasmonic absorption, but spherical Au nanoparticles (NPs) have the plasmonic feature is outside the biotransparency window (520-560 nm)[14]. The plasmonic feature can be shifted toward this window by engineering complex structures such as SiO_2@Au core-shells [17,18] or anisotropic nanorods [19], but the core-structures are oversized for biological use (typically, larger than 100-150 nm), while the anisotropic shape of the nanorods should be stabilized by non-biocompatible surfactants (e.g., CTAB).

Titanium nitride (TiN) NPs present an alternative plasmonic material, which is capable of providing a red-shifted peak around 650–800 nm [20,21] with a high photothermal conversion efficiency [21]. The possibility of using TiN NPs as the photothermal agent in cancer therapy and the contrast agent for bioimaging has already been justified [22,23], but their biomedical applications have been very limited so far due to the difficulty of fabricating stable water-dispersible solutions of clean TiN NPs via conventional chemical or plasma synthesis routes. We recently demonstrated the solution to this problem by using methods of laser ablation in liquid ambiance [24]. In this approach, a TiN target is ablated by laser radiation in water or organics (ethanol, acetone), which leads to the formation of colloidal TiN NPs solutions stabilized by a negative charge of the NPs (NPs prepared in organic solutions can be easily transferred to water). Profiting from a strong and broad plasmonic absorption band with its peak around 700 nm and a long tail over 800 nm, laser-synthesized TiN NPs demonstrated a strong phototherapy effect excited by 800 nm laser radiation [24]. A series of tests *in vitro* and *in vivo* showed that these NPs have a very low toxicity profile to confirm their safety, while the coating of NPs with polyethylene glycol (PEG) makes possible their prolonged circulation in the bloodstream and an efficient passive accumulation in a tumor via EPR effect [25]. Furthermore, examining laser-synthesized TiN NPs by combined optical and acoustic Z-scan technique, we recently observed a strong plasmon-mediated nonlinear absorption (NLA) effect [26], similar to what was earlier observed with Au NPs [27], which promises the development of bioimaging modality based on this nanomaterial.

Here, we experimentally demonstrate the possibility of nonlinear imaging using laser-synthesized TiN NPs as an exogenous contrast agent for PAM in the first (NIR I) biological window. We also show that the observed contrast is due to two-photon absorption (TPA) of TiN NPs.

TiN nanoparticles were synthesized by methods of femtosecond (fs) laser ablation methodology from a solid TiN target (GoodFellow, hot pressed, 99.5% purity) in acetone, as earlier described in [24]. Briefly, a focused beam from a Yb:KGW laser (1030 nm, 270 fs pulse length, 100 μJ pulse energy, 10 kHz repetition rate, TETA 10 model, Avesta, Russia) was used to ablate the target for 20 min. The obtained nanoparticle concentration was measured to be 57 μg/ml by employing the gravimetric method. The morphological analysis of the obtained NPs was carried out using a transmission electron microscope (TEM, model JEOL JEM-2010, LaB6 filament, 200 kV, 0.23 nm point to point resolution). Prior to TEM imaging, 10 μl of TiN NPs in acetone solution was dropped onto the carbon-coated copper grid (200 mesh, Oxford Instruments) and dried. The optical absorption characterization of TiN NP/Acetone sample was carried out by UV-Vis-NIR spectrophotometer.

Photoacoustic characterization of TiN NPs was carried out using a customized lab-made PAM setup, as shown in Fig. 1. An optical parametric oscillator (OPO) (OPOTEK, Vibrant 355 LD, 410 nm – 2.4 μm, 5 ns) operating at 20 Hz was employed as an optical source. The average diameter of the laser beam at its focus was measured to be ~ 50 μm. The sample was placed inside a distilled water cell, which was kept above the motorized two-axis (X-Y) translation stage. The photoacoustic (PA) signal from the sample was detected using a 5 MHz water immersion ultrasonic transducer (UST) (Olympus V310-N-SU), whose bandwidth limited the axial resolution [9]). For PA characterizations, a medical PVC (acoustic impedance of 3.2 x 10^6 rayls [28]) tube (an IV Infusion set) was first chosen for filling TiN NPs, which was found to be rapidly corroded by the acetone media. Therefore, a non-reactive cylindrical glass (acoustic impedance of 13 x 10^6 rayls [29]) capillary tube (PRECISION, China) having an internal (external) diameter of 1 mm (1.5 mm), and a length of 75 mm was selected to fill the TiN NPs solution. Prior to solution injection, the tube was cleaned via multiple acetone rinsing. The tube ends were sealed with a thermoplastic adhesive. The tube was attached to a plastic sample holder.

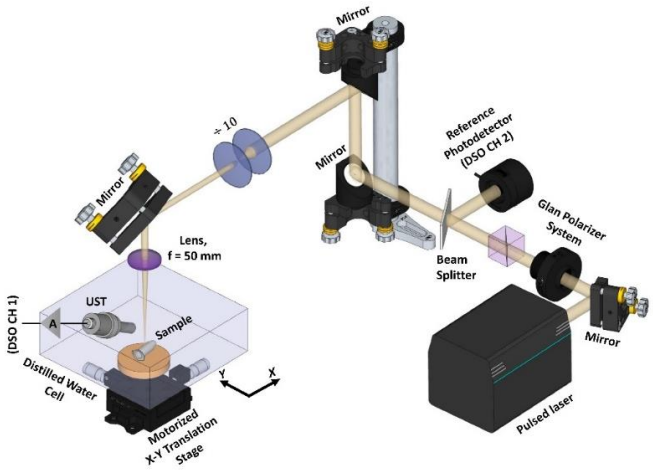

FIG. 1. Schematic representation of the photoacoustic microscopy setup. Laser energy is controlled by two Glan polarizers and a small part of the beam is directed to Channel 2 (CH 2) of a digital storage oscilloscope (DSO) via a reference photodetector to trigger the data acquisition. After a size reduction down to 500 μm diameter, the remaining beam is focused on the sample via a 50 mm convex lens. x-y translation of the sample is enabled by two 50 mm linear stages (MTS50-Z8 - 50 mm, Thorlabs Inc.). PA signal is amplified by a low noise amplifier (ZFL-500LN-BNC) with a gain of 19.4 and is fed to Channel 1 (CH 1) of the DSO.

Fig. 2(a) shows the morphology and size distribution of laser-synthesized TiN NPs. It is visible that the NPs were spherical with an averaged (mode) size of about 25 nm. An optical absorption spectrum of such NPs is shown by a solid blue line in Fig. 2(b). One can see that two remarkable absorption bands were present: a sharp transition below 400 nm associated with TiN band-to-band absorption, and a broad absorption band with a maximum at 700 nm, which is typically attributed to localized plasmon resonance (LPR) excited over TiN NPs [20,21]. In Fig. 2(b), a PA spectrum from TiN NPs (showed by red squares) is directly compared with its optical absorbance profile. Since the PA signal is directly proportional to the optical absorption of the sample, the PA spectrum follows its optical absorbance profile, with the peak

intensity reached at the same wavelength. However, one can notice a deviation of the PA spectrum with respect to its absorbance profile. There are published reports where the PA spectrum hugely differed from the optical absorbance nature [30–32]. The reports attribute such deviation to two important factors: (a) The involvement of different types of optical illumination sources (continuous/pulsed) and photophysical processes in the optical absorption and PA spectroscopy technique [30,32], and (b) domination of the non-linear effects in a material at higher optical fluence[31]. In our case, the presence of plasmonically enhanced two-photon absorption (TPA) at 725 nm (confirmed from Fig. 3(b)) is considered to be the principal reason for a deviation in the PA spectrum for TiN NPs in Fig. 2(b).

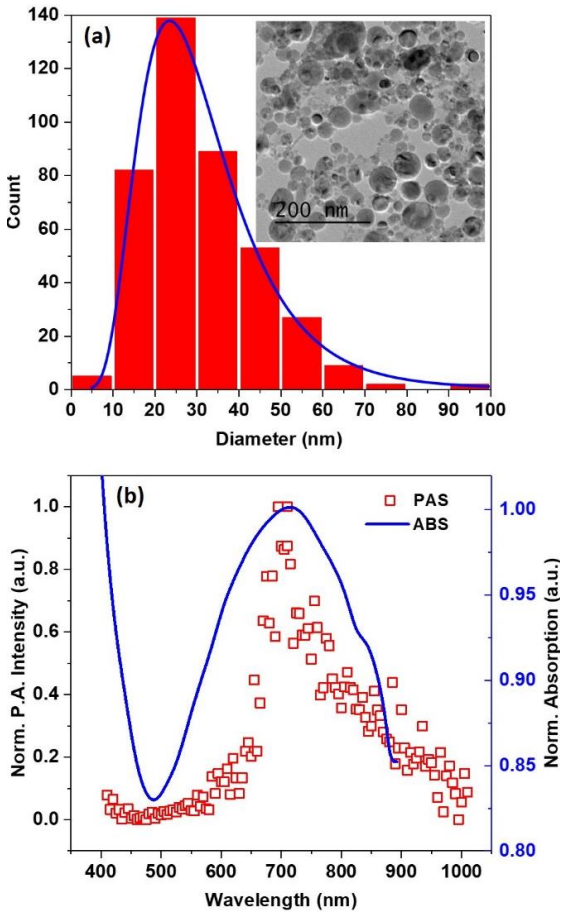

FIG. 2. (a) Typical TEM image of TiN NPs prepared by fs laser ablation in acetone (inset) and corresponding size distribution, (b) Comparative plot of absorbance and photoacoustic (PA) spectra of TiN NPs in acetone. PA spectroscopy is performed with 5 ns, 10 Hz tunable OPO laser. The amplitudes are normalized with respect to the plasmonic peak.

To check the dependence of PA signal intensity on the concentration of TiN NPs in acetone, a sample having 57 µg/ml concentration was diluted to its 20 %, 25 %, 33.3 %, and 50 % value, and corresponding PA intensity was recorded under a constant beam fluence of 1.85 mJ/cm^2 at 725 nm excitation, as shown in Fig. 3(a). As shown in the figure, PA intensity is linearly proportional to NPs concentration. A linear fitting to it provides an average slope of 8.38 without any nonlinearity or PA saturation effect.

Theoretically, the lateral resolution of PAM is given by the spot size of the optical focus [9], which was measured to be ~ 50 µm for our PAM setup. To determine the experimental value of resolution, a sharp-edged black colored pattern on a plastic sheet was imaged with 532 nm excitation as shown in Fig. 4(a). The measured PA profile was fitted to an edge spread function (ESF) and its first order derivative provided the line spread function (LSF) as shown in Fig. 4(a). The lateral resolution of the PAM was estimated from the full width at half-maximum (FWHM) of the corresponding LSF [33], which was about 67 µm.

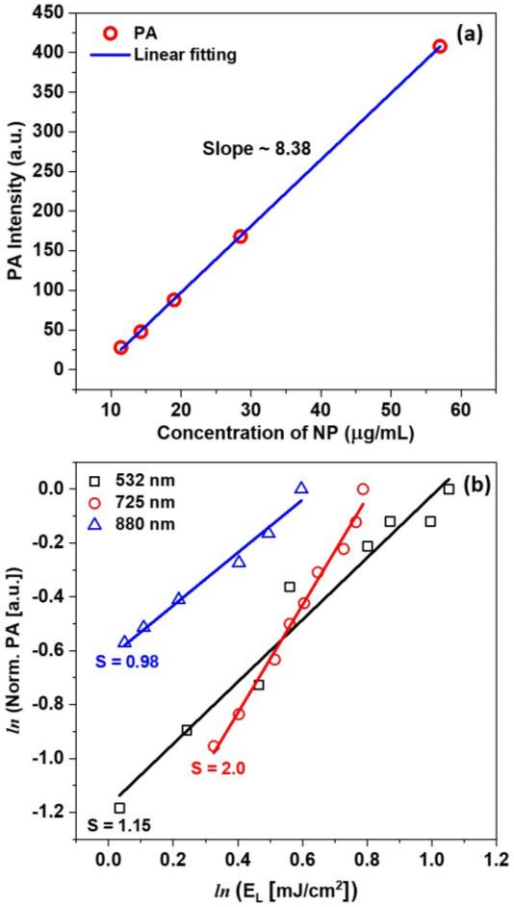

FIG. 3. (a) PA signal intensity as a function of TiN NPs concentration measured with 1.85 mJ/cm^2, 725 nm, 5 ns, 20 Hz tunable OPO laser, (b) ln-ln plot of normalized PA intensity of TiN NPs vs. laser fluence for different plasmonic wavelengths.

As a proof-of-concept for the use of TiN NPs as an exogenous agent contrast in a PAM imaging setup, images were generated for three different excitation wavelengths with the acetone TiN NPs suspension in a capillary tube, as shown in Figs. 4 (b), (c), and (d). The OPO laser employed in this work offers a maximum fluence of 1.85 mJ/cm^2 for 880 nm wavelength, therefore all the PAI are recorded keeping this energy density constant. Since the average diameter of the laser beam at its focus

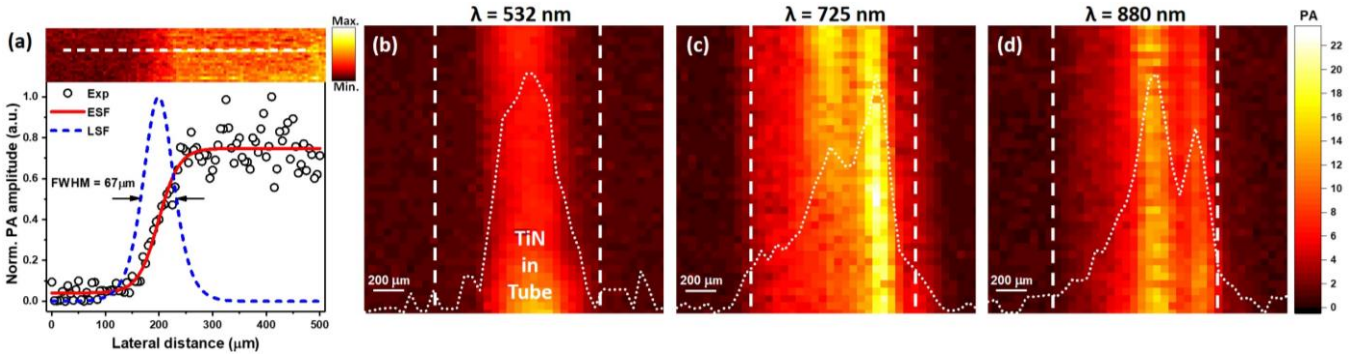

FIG. 4. (a) PAI of a sharp-edged black colored pattern on a plastic sheet and lateral resolutions of the PAI system. White dashed cut-line profile on PAI is used for obtaining ESF and LSF. PAI of TiN NPs in acetone placed in capillary tube under an excitation wavelength of (b) 532 nm, (c) 725 nm, and (d) 880 nm, performed with 1.85 mJ/cm^2 illumination, 20 Hz, 5 ns. False dashed lines indicate boundaries. The dotted line represents normalized horizontal cut-line spatial profile at y-axis = 1.0 mm. EXP: experimental PA values, ESF: edge spread function, and LSF: line spread function.

is ~ 50 μm, the scan step size or the pixel dimension is fixed to 50 μm on both the X and Y-axis. This step size eliminates any pixel overlapping which occurs due to beam size mismatch. Such scanning covers the whole 2D PAI frame with 40 x 40 pixels.

The obtained images display, from their qualitative intensity behavior (see the false color scale on the right-hand side) that the highest intensity occurs at the plasmonic absorption peak wavelength, followed by a less intensity image at 880 nm and the lowest intensity for excitation at 532 nm. The dashed lines indicate the capillary tube lateral boundary, with a dimension of ~1 mm. It should also be noted that the highest intensity (yellowish) in Fig. 4(c) and (d) are not centered due to the position of the photoacoustic detector at a slight angle from the direct light beam incidence. For the lowest emitted PA signal at 532 nm excitation, it can also be seen that the spatial profile at its FWHM is ~ 453 μm. Similarly, for the 725 nm and 880 nm excitations, the spatial profile at its FWHM is ~ 518 μm and ~ 511 μm, respectively.

The generation of TPA-induced PA signal is well understood in terms of the two-photon excitation (TPE) and resultant non-radiative process upon photon absorption by the material. Since the TPE is a second-order process, the number of photons absorbed by a material per unit time N_{abs} depends on several factors including, the square of light fluence or energy density (E_L), the TPA cross-section $\sigma^{(2)}$, the material (NPs in this work) concentration C and the effective volume V under two-photon illumination, and can be expressed as [34,35]:

$$N_{abs}(t) = \int_V dV \sigma^{(2)} C(\boldsymbol{r}, t)\, E_L^2(\boldsymbol{r}, t) \qquad (1)$$

where r and t signify respective spatial and temporal components. Following the mathematical treatment of equation (1) [34,35], one can arrive at the following equation for the spatial distribution of PA signal:

$$PA(\boldsymbol{r}) \cong \left\{\frac{1}{2}(1-\eta_2)\Gamma C S^2 E_{tr} \rho(\boldsymbol{r}) \sigma^{(2)}\right\} E_L^2 \qquad (2)$$

In equation (2), the term $(1-\eta_2)$ describes the nonradiative efficiency of the material, Γ is the Grüneisen parameter, which indicates the efficiency of conversion of absorbed optical energy to acoustic pressure, S is the spatial distribution of the incident laser fluence, E_{tr} is the transferred optical energy to heat energy, and $\rho(\boldsymbol{r})$ is the density, in which absorption occurs. This equation indicates a quadratic dependence of the PA signal on the incident laser fluence in a two-photon process, as expected.

To confirm the presence of the TPA effect for TiN NPs [26], or more precisely to prove that the PA signal in TiN NPs follows equation (1), the PA signal intensities were recorded with increasing laser fluence for different wavelengths. Since the LPR broadband covers ranges from visible to near-infrared regions (Fig. 2 b), three excitation wavelengths were selected: 532 nm, 725 nm, and 880 nm. Fig. 3(b) shows the ln-ln plot of the normalized PA intensity as a function of laser fluence for the three excitation wavelengths. Here, the PA amplitude normalization is carried out by dividing PA signal intensities (for each wavelength) by their respective maximal PA values. The linear fitting to such plots depicts the presence of plasmonically enhanced TPA with a slope of S = 2.0 for 725 nm excitation. However, the quadratic dependence is not evident for 532 nm and 880 nm excitation wavelengths, as the slope values are S = 1.15 and 0.98, respectively. This may be attributed to relatively low plasmonic absorption at these wavelengths, as confirmed by the spectroscopic results in Fig. 2(b).

Regarding the obtained images, it can be seen from Figs. 4 (b, c and d) that solutions of TiN NPs demonstrate significant PA signature for all three excitation wavelengths. The image contrast of PAI can be estimated using the Weber contrast W formula as [36]:

$$W = \frac{I_S - I_B}{I_B} \qquad (3)$$

where I_S is the intensity of the PA signal from the sample, whereas I_B is the similar quantity from the background. The Weber contrast is calculated to be 31.95, 69.41, and 31.03 for the excitation wavelength of 532 nm, 725 nm, and 880 nm, respectively. Nearly two-fold enhancement in PA contrast for 725 nm wavelength is attributed to the plasmonically enhanced TPA in TiN NPs, as confirmed by data presented in Fig. 2(b) and Fig. 3(b). The contrast values for 532 nm and 880 nm excitation match with each other and follow the optical absorption profile shown in Fig. 2(b). This again confirms that the PA intensity is directly proportional to the optical absorption in the nanoparticle. The lateral dimension of the tube measured from PAM is ~ 1 mm which matches with the specification of the capillary tube and, as mentioned before. The horizontal cut-line spatial profile to the

PAI images signify the lateral distribution of the PA intensities. It is to be noted that the TiN NPs are filled inside a cylindrical glass capillary tube. Naturally, the TiN volume will not be similar along the diameter. Moreover, equation (1) clearly states that the optical absorption by material and hence the PA signal is directly proportional to the volume of the nanoparticle. Therefore, the PA signal varies along the diameter of the tube for all the wavelengths as shown by the line profile in Fig. 4. The FWHM value for the 532 nm excitation is comparatively smaller than others which is attributed to the relatively lower PA intensity at this wavelength which is depicted in PA spectrum in Fig. 2(b).

The observation of a strong nonlinear photoacoustic response associated with plasmonically-enhanced two-photon absorption from laser-synthesized TiN NPs opens up an attractive avenue for the employment of these nanoparticles as contrast agents in photoacoustic biological imaging. Here, the demonstrated high PA contrast and high (67 μm) resolution of PA images promises the use of such NPs in different PA modalities, including photoacoustic microscopy (PAM) and photoacoustic tomography (PAT). It is important that owing to a broad plasmon-related absorption band (maximum at 700 nm) TiN nanoparticles provide the strongest PA signal in the region of relative tissue transparency (630-900 nm), which promises their efficient use *in vivo*. Furthermore, such absorption is generated by 20-30 nm TiN NPs, which are much smaller than Au-based nanostructures (core-shells, nanorods) used in similar tasks, which are typically larger than 100-150 nm [17–19] Such a small size of TiN NPs is critically important to ensure good transport *in vivo* and subsequent excretion of NPs[37]. As we showed in previous study [24], the size of laser-synthesized TiN NPs can be further reduced down to 4-5 nm, but such small NPs are still capable of providing plasmonic features in the biological transparency window. It should be noted that in this study we demonstrated the feasibility of nonlinear photoacoustic imaging profiting on plasmonic absorption of TiN NPs placed in acetone solutions. As we showed in Ref [25], TiN NPs can be easily transferred from acetone to water and then coated by polyethylene glycol (PEG) with a minimal loss plasmonic absorption intensity (less than 5%) and the conservation of spectral position of the plasmonic peak. Based on almost complete match of absorption spectra from these samples, one can expect the same efficiency of aqueous solutions of TiN NPs in photoacoustic imaging tasks. Photoacoustic imaging experiments in biological models are now in progress and will be published elsewhere. Another advantage of the used NPs consists in the absence of toxic impurities as a result of clean laser-ablative synthesis. It should be noted that the cleanness of nanomaterials is one of the main trademarks of laser-ablative technology. Such a cleanness makes possible high biocompatibility, which was previously demonstrated for a variety of nanomaterials, including Si [38,39], Au [40], Bi [41] , and B [42] NPs. As we showed in our recent study [25], laser-synthesized TiN NPs are highly safe, which was demonstrated in a variety of tests *in vitro* and *in vivo*. We also showed that the coating of NPs by PEG leads to a substantial prolongation of circulation of laser-synthesized NPs and their enhanced accumulation in tumors. In this case, the proposed imaging modality based on non-linear PA response can be used to track the location of NPs in tissues, while an efficient heating effect under photoexcitation in the region of relative tissue transparency [24] can be applied to destroy cancer cells and achieve a therapeutic outcome. As another opportunity, we envision the use of TiN NPs as contrast agents for dental diagnostics in PAI and PAT modalities [43]. These experiments are now in progress.

In conclusion, we explored titanium nitride (TiN) NPs fabricated by methods of pulsed laser ablation in liquids as an exogenous contrast agent in PAI. The obtained results with PAM and PAS confirm the role of plasmonic enhancement in TPA in the nanoparticles. TiN NPs look advantageous over gold counterparts, since their plasmonic band occurs in the first biological window (NIR I), rendering possible a deeper optical penetration of exciting light for PAI generation. The improvement in axial and lateral resolution can be easily achieved by using appropriate focusing optics and a wider bandwidth acoustic detector. The proposed imaging technique can be combined with the phototherapy functionality of laser-synthesized TiN NPs and thus advance theranostic modality based on plasmonic nanomaterials.

ACKNOWLEDGEMENTS

This work was funded by INCT of Photonics Program supported by CNPq, CAPES and FACEPE (Grant 465.763/2014-6) for optical characterization and the Russian Science Foundation (Project 19-72-30012) for fabrication and characterization of TiN NPs.

AUTHOR DECLARATIONS

Conflict of Interest

The authors confirm the absence of conflicts of interest associated with this publication.

DATA AVAILABILITY

Data available on request from the authors

REFERENCES

[1] G. Pirovano, S. Roberts, S. Kossatz, and T. Reiner, J. Nucl. Med. **61**, 1419 (2020).
[2] L. Shi and R.R. Alfano, editors , *Deep Imaging in Tissue and Biomedical Materials* (Jenny Stanford Publishing, 2017).
[3] J. Tang, J. Ren, and K.Y. Han, Nanophotonics **8**, 2111 (2019).
[4] V. Parodi, E. Jacchetti, R. Osellame, G. Cerullo, D. Polli, and M.T. Raimondi, Front. Bioeng. Biotechnol. **8**, (2020).
[5] E.A. Swanson and J.G. Fujimoto, Biomed. Opt. Express **8**, 1638 (2017).
[6] P. Daukantas, Opt. Photonics News **31**, 32 (2020).
[7] L. Li, L. Lin, and L. V. Wang, Opt. Photonics News **29**, 32 (2018).
[8] L. V Wang and J. Yao, Nat. Methods **13**, 627 (2016).
[9] J. Yao and L. V. Wang, Laser Photon. Rev. **7**, 758 (2013).
[10] Q. Fu, R. Zhu, J. Song, H. Yang, and X. Chen, Adv. Mater. 1805875 (2018).
[11] N. Vogler, S. Heuke, T.W. Bocklitz, M. Schmitt, and J. Popp, Annu. Rev. Anal. Chem. **8**, 359 (2015).
[12] R.A.S. George I. Stegeman, *Nonlinear Optics: Phenomena, Materials and Devices* (Wiley, 2012).
[13] R. Gao, Z. Xu, Y. Ren, L. Song, and C. Liu, Photoacoustics **22**, 100243 (2021).
[14] P.K. Jain, K.S. Lee, I.H. El-Sayed, and M.A. El-Sayed, J. Phys. Chem. B **110**, 7238 (2006).
[15] J.E. Lemaster and J. V. Jokerst, WIREs Nanomedicine and Nanobiotechnology **9**, (2017).
[16] T. Lee, H.W. Baac, Q. Li, and L.J. Guo, Adv. Opt. Mater. **6**, 1800491

(2018).
[17] A.M. Gobin, M.H. Lee, N.J. Halas, W.D. James, R.A. Drezek, and J.L. West, Nano Lett. **7**, 1929 (2007).
[18] Y. Wang, X. Xie, X. Wang, G. Ku, K.L. Gill, D.P. O'Neal, G. Stoica, and L. V. Wang, Nano Lett. **4**, 1689 (2004).
[19] X. Huang, I.H. El-Sayed, W. Qian, and M.A. El-Sayed, J. Am. Chem. Soc. **128**, 2115 (2006).
[20] U. Guler, S. Suslov, A. V. Kildishev, A. Boltasseva, and V.M. Shalaev, Nanophotonics **4**, 269 (2015).
[21] A. Lalisse, G. Tessier, J. Plain, and G. Baffou, Sci. Rep. **6**, 38647 (2016).
[22] W. Jiang, Q. Fu, H. Wei, and A. Yao, J. Mater. Sci. **54**, 5743 (2019).
[23] W. He, K. Ai, C. Jiang, Y. Li, X. Song, and L. Lu, Biomaterials **132**, 37 (2017).
[24] A.A. Popov, G. Tselikov, N. Dumas, C. Berard, K. Metwally, N. Jones, A. Al-Kattan, B. Larrat, D. Braguer, S. Mensah, A. Da Silva, M.-A. Estève, and A. V. Kabashin, Sci. Rep. **9**, 1194 (2019).
[25] I. V. Zelepukin, A.A. Popov, V.O. Shipunova, G. V. Tikhonowski, A.B. Mirkasymov, E.A. Popova-Kuznetsova, S.M. Klimentov, A. V. Kabashin, and S.M. Deyev, Mater. Sci. Eng. C **120**, 111717 (2021).
[26] M.E. Maldonado, A. Das, A.S.L. Gomes, A.A. Popov, S.M. Klimentov, and A. V. Kabashin, Opt. Lett. **45**, 6695 (2020).
[27] W. Li and X. Chen, Nanomedicine **10**, 299 (2015).
[28] N. Yesiller, T. Edil, and C. Benson, Geotech. Test. J. **20**, 17 (1997).
[29] F.J. Álvarez Franco, in *Geogr. Fingerprinting Data to Creat. Syst. Indoor Position. Indoor/Outdoor Navig.* (Elsevier, 2019), pp. 335–351.
[30] Y. Jiang, P.K. Upputuri, C. Xie, Y. Lyu, L. Zhang, Q. Xiong, M. Pramanik, and K. Pu, Nano Lett. **17**, 4964 (2017).
[31] A. Danielli, K. Maslov, C.P. Favazza, J. Xia, and L. V. Wang, Appl. Phys. Lett. **106**, 203701 (2015).
[32] K. Pu, A.J. Shuhendler, J. V. Jokerst, J. Mei, S.S. Gambhir, Z. Bao, and J. Rao, Nat. Nanotechnol. **9**, 233 (2014).
[33] P. Hai, J. Yao, K.I. Maslov, Y. Zhou, and L. V. Wang, Opt. Lett. **39**, 5192 (2014).
[34] B.E. Urban, J. Yi, V. Yakovlev, and H.F. Zhang, J. Biomed. Opt. **19**, 085001 (2014).
[35] C. Xu and W.W. Webb, J. Opt. Soc. Am. B **13**, 481 (1996).
[36] L. Yu, J. Sun, X. Lv, Q. Feng, H. He, B. Zhang, Y. Ding, and Q. Liu, Sci. Rep. **9**, 17262 (2019).
[37] G. Chen, I. Roy, C. Yang, and P.N. Prasad, Chem. Rev. **116**, 2826 (2016).
[38] T. Baati, A. Al-Kattan, M.-A. Esteve, L. Njim, Y. Ryabchikov, F. Chaspoul, M. Hammami, M. Sentis, A. V. Kabashin, and D. Braguer, Sci. Rep. **6**, 25400 (2016).
[39] V.M. Petriev, V.K. Tischenko, A.A. Mikhailovskaya, A.A. Popov, G. Tselikov, I. Zelepukin, S.M. Deyev, A.D. Kaprin, S. Ivanov, V.Y. Timoshenko, P.N. Prasad, I.N. Zavestovskaya, and A. V. Kabashin, Sci. Rep. **9**, 2017 (2019).
[40] A.-L. Bailly, F. Correard, A. Popov, G. Tselikov, F. Chaspoul, R. Appay, A. Al-Kattan, A. V. Kabashin, D. Braguer, and M.-A. Esteve, Sci. Rep. **9**, 12890 (2019).
[41] J.C. Bulmahn, G. Tikhonowski, A.A. Popov, A. Kuzmin, S.M. Klimentov, A. V. Kabashin, and P.N. Prasad, Nanomaterials **10**, 1463 (2020).
[42] A.I. Pastukhov, I.B. Belyaev, J.C. Bulmahn, I. V. Zelepukin, A.A. Popov, I.N. Zavestovskaya, S.M. Klimentov, S.M. Deyev, P.N. Prasad, and A. V. Kabashin, Sci. Rep. **12**, 9129 (2022).
[43] E.J. da Silva, E.M. de Miranda, C.C.B. de O. Mota, A. Das, and A.S.L. Gomes, Imaging Sci. Dent. **51**, 107 (2021).